Mesoporous TiO₂ Single Crystals: Facile Shape-, Size-, and Phase-Controlled Growth and Efficient Photocatalytic Performance

Xiaoli Zheng, Qin Kuang, Keyou Yan, Yongcai Qiu, Jianhang Qiu, and Shihe Yang*

Department of Chemistry, The Hong Kong University of Science and Technology, Clear Water Bay, Kowloon, Hong Kong

S Supporting Information

ABSTRACT: In this work, we have succeeded in preparing rutile and anatase TiO₂ mesoporous single crystals with diverse morphologies in a controllable fashion by a simple silica-templated hydrothermal method. A simple in-template crystal growth process was put forward, which involved heterogeneous crystal nucleation and oriented growth within the template, a sheer spectator, and an excluded volume, i.e., crystal growth by faithful negative replication of the silica template. A series of mesoporous single-crystal structures, including rutile mesoporous TiO₂ nanorods with tunable sizes and anatase mesoporous TiO₂ nanosheets with dominant {001} facets, have been synthesized to demonstrate the versatility of the strategy. The morphology, size, and phase of the TiO₂ mesoporous single crystals can be tuned easily by varying the external conditions such as the hydrohalic acid condition, seed density, and temperature rather than by the silica template, which merely serves for faithful negative replication but without interfering in the crystallization process. To demonstrate the application value of such TiO₂ mesoporous single crystals, photocatalytic activity was tested. The resultant TiO₂ mesoporous single crystals exhibited remarkable photocatalytic performance on hydrogen evolution and degradation of methyl orange due to their increased surface area, single-crystal nature, and the exposure of reactive crystal facets coupled with the three-dimensionally connected mesoporous architecture. It was found that {110} facets of rutile mesoporous single crystals can be considered essentially as reductive sites with a key role in the photoreduction, while {001} facets of anatase mesoporous single crystals provided oxidation sites in the oxidative process. Such shape- and size-controlled rutile and anatase mesoporous TiO₂ single crystals hold great promise for building energy conversion devices, and the simple solution-based hydrothermal method is extendable to the synthesis of other mesoporous single crystals beyond TiO₂.

KEYWORDS: mesoporous single crystal, TiO₂, controllable crystal growth, photocatalysts
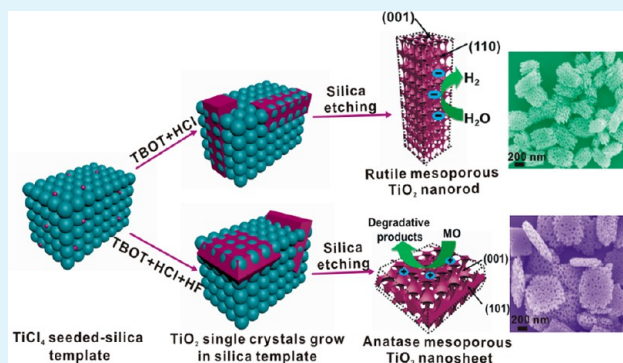
■ INTRODUCTION

The mesoporous framework of metal oxides with single crystallinity has attracted great interest due to its high surface area, good thermal and mechanical stability, and superior charge-transport capability.[1−3] These intriguing merits endow high potential to the mesoporous single crystals of metal oxides in wide ranging areas from power generation to energy conversion.[4−8] To date, many templating strategies, including soft-[9−15] and hard-templated approaches,[16−23] have been widely employed to construct mesoporous structures. However, the soft-templated method requires complicated control of the assembly processes and normally results in mesoporous materials in amorphous or semicrystalline phases.[9,24] By contrast, the hard-templated method has been considered as a general route to produce (mono)crystalline mesoporous materials using presynthesized mesoporous silica or carbon as templates.[25−28] Among the remaining problems is the difficulty to completely fill the mesopores of the hard template, leading to the tendency of framework collapse after template removal.[5]

As a wide-band-gap semiconductor, titanium oxide (TiO₂) has been extensively studied as an attractive material for

photocatalysis, solar cell, water splitting, and battery devices.[29−31] Importantly, the performance of those devices is heavily dependent on the surface area, crystallinity, and the exposure of reactive crystal facets.[32−35] Mesoporous TiO₂ made up of preformed nanocrystals with high surface area has been well developed recently,[36−40] but possible carrier trapping or recombination at grain boundaries may significantly decrease device performance. Therefore, building long-range crystalline order becomes equally important as the mesoporous control to ensure the overall high device performance.[40] Recently, a series of novel rutile and anatase TiO₂ single crystals with tunable exposed facets have been prepared and investigated for a vast range of applications.[41−44] However, the application scope of the as-made TiO₂ single crystals is clearly limited by their low surface areas, especially for the large sized single crystals. In this sense, it is important to build networks of pores within the single crystals to preserve the structural coherence for long-

range charge transport and to provide a large amount of highly accessible surfaces for the desired physical or chemical processes to enhance the pore-dependent performance.[45]

Recently, synthesis of mesoporous monocrystalline TiO_2 has been achieved by silica-templated thermolysis or hydrothermal methods.[46,47] Interestingly, the hydrothermal method yielded anatase mesoporous TiO_2 single crystals (A-MSCs) with well-defined facets, which delivered enhanced carrier mobility relative to TiO_2 nanoparticle film.[47] Compared to anatase TiO_2, rutile TiO_2 is known to have additional advantages including better chemical stability, higher refractive index, and higher lithium insertion capacity.[48,49] However, there have been no reports about the fabrication of rutile mesoporous TiO_2 single crystals (R-MSCs) with well-defined facets in a delicately controllable way. Therefore, it is necessary to extend the templating strategy to synthesize such mesoporous single crystals. More generally, it is important to understand the mechanisms behind the templating strategy. Simply regarding the template as a reaction media, some important questions up in the air are: how different is the templating reaction process in it from that in a solution? Can shape-, size-, and phase-controls be achieved for the nanocrystal synthesis in such reaction media as in a solution?

The present study aims to address the questions and the like. Toward this direction, we successfully prepared R-MSCs and A-MSCs with diverse morphologies in a controllable fashion by a simple silica-templated hydrothermal method. It was found that the morphology, size, and phase of the TiO_2 MSCs can be tuned easily by varying the external conditions such as the hydrohalic acid condition, seed density, and temperature. A series of interesting mesoporous single-crystal structures, including rutile mesoporous TiO_2 nanorods with tunable sizes and anatase mesoporous TiO_2 nanosheets with dominant {001} facets, had been synthesized to demonstrate the versatility of our strategy. To our knowledge, this is the first report on shape-, size-, and phase-controlled preparation of R-MSCs and A-MSCs. To demonstrate the application value of such TiO_2 MSCs, photocatalytic activity was tested. The obtained TiO_2 MSCs were found to exhibit remarkable photocatalytic performance thanks to the single-crystal structure and the exposure of reactive crystal facets coupled with the three-dimensionally connected mesoporous architecture.

■ EXPERIMENTAL SECTION

Preparation of Seeded Silica Templates. Seeded silica templates were prepared according to a literature procedure with some modifications.[47] First, ~50 nm silica spheres (see Figure S1 in the Supporting Information) were synthesized by mixing 10.6 mL of H_2O (18.2 MΩ, Millipore Milli-Q), 6 mL of ammonium hydroxide (28%, VWR International S.A.S.), and 250 mL of ethanol (≥99.9%, Merck) in a 500 mL three-neck flask at room temperature. Next, 33 mL of tetraethyl orthosilicate (98%, Aldrich) was added in the flask quickly, and the mixture was stirred for 24 h. Then the product was centrifuged at 7000 rpm for 1 h, and the translucent solid was collected and sintered at 500 °C for 30 min (ramping time 150 min).

The silica templates were seeded by titanium tetrachloride ($TiCl_4$, ≥99%, Aldrich) aqueous solutions (0.03−15 mM), which were prepared from aqueous dilution of 2 M $TiCl_4$ stock solution. An amount of 5 g of the sintered silica template was put in 30 mL of $TiCl_4$ solution and seeded at 70 °C for 1 h. Then the template was rinsed with 1 L of H_2O and resintered at 500 °C for 30 min (ramping time 150 min).

Synthesis of R-MSCs and A-MSCs. TiO_2 MSCs were synthesized by a silica-templated hydrothermal method. For the R-MSCs, 14 mL

of deionized water was mixed with 14 mL of concentrated hydrochloric acid (HCl, 37%, VWR International S.A.S) in the Teflon-lined stainless steel autoclaves (50 mL volume). The mixture was stirred at room temperature for 10 min before adding 0.4 mL of titanium butoxide (TBOT, 97%, Aldrich). After stirring for another 10 min, 360 mg of the seeded silica template was added in the autoclave. Then, the sealed vessel was heated at 150−200 °C for 12 h in an oven. Afterward, the vessel was cooled to room temperature naturally, and the solid particles settled at the bottom were collected. Then the solid particles were washed with a large amount of water by vacuum filtration. Finally, the silica template was removed by etching in 2 M NaOH at 80 °C for 1 h. Then the remaining TiO_2 products were collected by centrifugation and washed with H_2O and ethanol several times. The A-MSCs with a high percentage of exposed {001} facets were prepared by adding 0.05 M hydrofluoric acid (HF, 50%, Aldrich) in the HCl aqueous solution, and the following procedures were the same as that for the preparation of R-MSCs. In the control experiments, solid TiO_2 single crystals were prepared in the same hydrothermal system without the addition of seeded silica template.

Evaluation of Photocatalytic Activity for Hydrogen (H_2) Evolution and Methyl Orange (MO) Degradation. The H_2 evolution experiments were carried out in a commercial water splitting measurement system (Labsolar-III, Beijing Perfect light Technology Co., Ltd.). First, 30 mg of the obtained TiO_2 sample was dispersed in 10 mL of methanol aqueous solution (30 v/v %) by ultrasonication for 10 min, and then an aqueous H_2PtCl_6 solution (76.8 μL, 0.02 mol·L^{-1}) was added into the mixture under magnetic stirring for 30 min. Next, the suspension was illuminated under a 300 W Xe lamp (PLS-SXE-300UV) for 30 min, to in situ photodeposit Pt nanoparticles (Pt NPs) as cocatalyst for photocatalytic hydrogen evolution. The color of the suspension turned gray, indicating successful loading of Pt NPs on the TiO_2 samples. Next, the suspension was transferred into a reaction chamber under cooling circulation at 5 °C, and another 90 mL of methanol solution (30 v/v %) was added under stirring. Then the chamber was sealed and evacuated to remove the air. Under irradiation of the 300 W Xe lamp (with the wavelength of 320−780 nm), the evolved gases were detected by online gas chromatography.

Photodegradation of MO (50 mL, 4×10^{-5} M) was carried out in the reaction chamber under cooling circulation at 20 °C in the presence of TiO_2 photocatalysts (10 mg) under illumination of a 300 W Xe lamp (with the wavelength of 320−780 nm). The mixture of TiO_2 in a MO solution was stirred in the dark at ambient temperature for 1 h to ensure adsorption−desorption equilibrium. Upon equilibrium, 2 mL of the suspension was extracted out to determine the initial concentration of MO solution, which was recorded as the base concentration C_0. Then, the remaining mixture was illuminated with a 300 W Xe lamp, and 2 mL of the suspension was extracted out at a series of time intervals. Next, the extracted suspensions were centrifuged to separate any suspended solid. UV−vis spectra of the upper supernatant were measured using a Hitachi 3010 UV−vis spectrophotometer to determine the concentration of the remaining MO as a function of reaction time, which is designated as C.

Characterization. Morphology analysis was performed on a scanning electron microscope (SEM, JEOL 6700F) at an accelerating voltage of 5 kV. More detailed structural examinations were carried out by transmission electron microscopy (TEM, JEOL 2010F) and high-resolution TEM with an accelerating voltage of 200 kV. X-ray photoelectron spectroscopy (XPS) was carried out by a Kratos Axis Ultra DLD multitechnique surface analysis system. Powder X-ray diffraction (XRD) patterns were recorded on a Philips high-resolution X-ray diffraction system (model PW1830) with Cu Kα radiation (λ = 1.5406 Å). Brunauer−Emmett−Teller (BET) surface areas and nitrogen adsorption−desorption isotherms of the samples were measured by a Coulter SA 3100 surface area analyzer. UV−vis spectra were measured by a Hitachi 3010 UV−vis spectrophotometer.

■ RESULTS AND DISCUSSION

Formation of the Rutile and Anatase Mesoporous TiO_2 Single Crystals. Scheme 1 illustrates the growth

Scheme 1. Schematic Illustration of the Growth Pathways of R-MSCs and A-MSCs in the Silica Template by a Hydrothermal Method
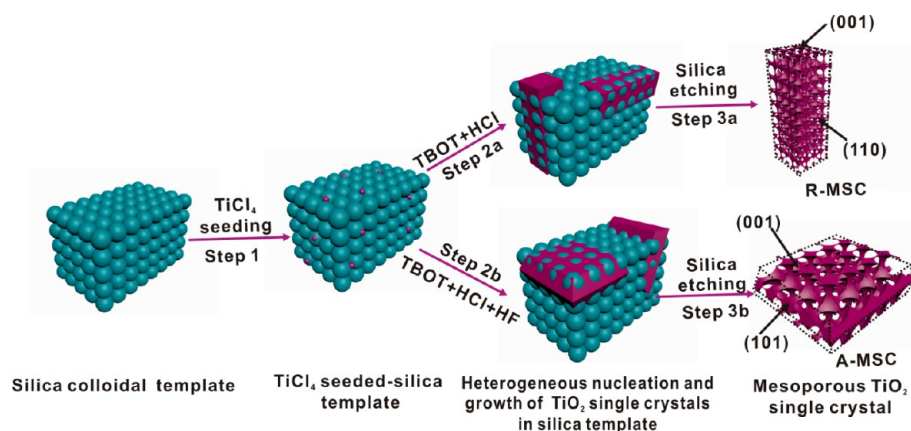
processes of R-MSCs and A-MSCs in the silica template by hydrothermal treatment. By changing the reaction conditions during the crystal growth process, it is in principle feasible to control the structures and phases of the final TiO$_2$ crystals. We chose hydrohalic acid solutions (HCl and HF) as the reaction media because they could act as a morphology controlling agent to effectively fabricate single crystals with preferred crystal facets and phases.[42,43] At high concentrations of HCl, TiO$_2$ prefers to form a [001]-oriented tetragonal rutile nanorod because HCl works like a catalyst to lower the activation energy for the rutile formation (step 2a).[42,50] Differently, a small quantity of HF can act as a capping agent to evolve anatase TiO$_2$ nanosheets with predominant {001} facets (step 2b).[43,51] Owing to the quasi-close packing of the silica template, R-MSCs and A-MSCs, after negatively replicating the template, can be obtained by removing the silica sphere template (step 3). Taken together, the shape-, size-, and phase-controlled MSCs can be prepared by the combination of careful preseeding, tuning of the in-template growth, and post-template removal.

To implement the aforementioned concept in the synthesis of mesoporous single crystals, we performed hydrothermal treatment of TBOT in hydrohalic acid reaction media. As shown in Figure 1 (a1 without HF and b1 with HF), solid tetragonal TiO$_2$ nanorods (average width of ∼350−400 nm and length of ∼2.5−3 μm) and highly truncated bipyramid-shaped nanosheets (average width of ∼2 μm and thickness of ∼350 nm) were obtained in aggregated states when the silica template was not used. In the presence of the silica template, however, homogeneously dispersed mesoporous TiO$_2$ nanorods (Figure 1(a2), without HF) (average width of ∼300−400 nm and length of ∼500−600 nm) and nanosheets (Figure 1(b2), with HF) (average width of ∼700−800 nm and thickness of ∼150 nm) were obtained with mesopores (diameter ∼50 nm) negatively replicating the removed silica template. It appears that the seeded silica template could provide a more effective crystal growth environment than the solution for fixing the crystals in place and avoiding their aggregation. The overall morphologies of the MSCs have largely retained those of the solid TiO$_2$ nanostructures under the respective reaction conditions due to the specific halogen-dependent surface-selective stabilization effect.

The phase identity and purity of the solid and mesoporous TiO$_2$ were verified by XRD patterns, and the results were shown in Figure 2. The mesoporous nanorods give an XRD
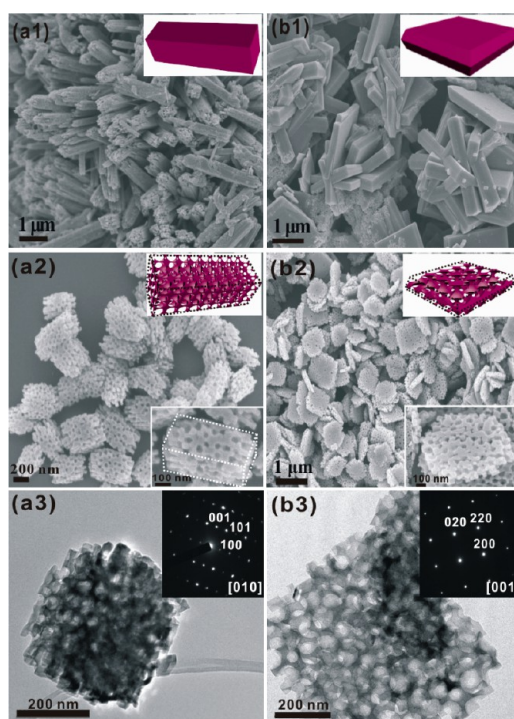

Figure 1. SEM images of solid (a1) TiO$_2$ nanorods and (b1) TiO$_2$ nanosheets prepared without SiO$_2$ template. (a2, b2) SEM images and (a3, b3) TEM images of mesoporous TiO$_2$ short nanorods (a2, a3) and mesoporous TiO$_2$ nanosheets (b2, b3). Seeding concentration: 0.3 mM, 180 °C, 12 h. The corresponding selected-area electron diffraction (SAED) patterns were shown in the insets. Left panels (a): no HF. Right panels (b): [HF] = 0.05 M.

pattern that agrees well with the standard rutile TiO$_2$ (JCPDS No. 76-0319), whereas the mesoporous nanosheets are in the phase of anatase TiO$_2$ (matching the standard pattern of JCPDS No. 84-1285). Importantly, the sharp diffraction peaks and absence of impurity peaks indicate the high crystallinity and high purity of the mesoporous TiO$_2$. Finer details of the mesoporous nanorods and nanosheets were provided by the TEM images in Figure 1, which show evenly distributed mesopores with a uniform diameter of ∼50 nm, forming a connected network by channels 10−20 nm wide throughout the whole framework. The corresponding SAED patterns shown in the insets display the single crystalline nature of the
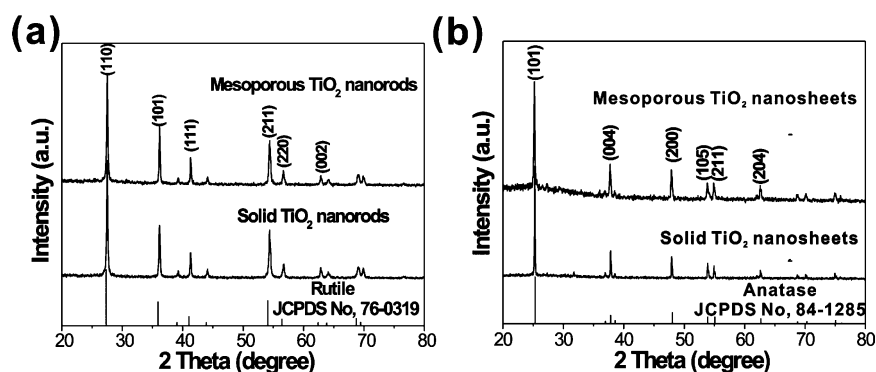
Figure 2. XRD patterns of (a) solid and mesoporous rutile TiO_2 nanorods in the absence of HF and (b) solid and mesoporous anatase TiO_2 nanosheets in the presence of HF.

mesoporous TiO_2 products, wherein [001]-oriented tetragonal R-MSCs (Figure 1(a3) without HF) with dominant {110} facets and A-MSCs (Figure 1(a3) with HF) with dominant {001} facets are successfully prepared with the silica-templated hydrothermal method. In addition, the XPS spectra of the A-MSCs shown in Figure S2 (Supporting Information) manifest the existence of F 1s core electrons at the binding energy of 684.5 eV, which is typical of the Ti−F species on the TiO_2 {001} crystal surface and clearly arises from our HF treatment process.[43] Therefore, we have proved that the hydrohalic acid media could act as effective morphology and phase controlling agents for the preferential formation of R-MSC nanorods and A-MSC nanosheets with well-defined facets in much the same way as for the synthesis of the corresponding solid TiO_2 nanostructures.

The control over the crystal structure and facets of TiO_2 single crystals has been extensively investigated.[52,53] It has been found that hydrohalic acids (HCl and HF) can not only modulate the phase transformation between rutile and anatase but also control the facets of the crystals. The key relates to the differences in the structure of the two polymorphs: in rutile, $[TiO_6]$ octahedra associate by sharing edges along the c axis and then by corner-sharing to form the three-dimensional framework, whereas in anatase, the $[TiO_6]$ octahedra are joined together all with edge-shared bonding throughout the three-dimensional framework.[54] In the presence of concentrated HCl, a high concentration of H+ (acidic) strongly protonates the surface of $[TiO_6]$ octahedra and effectively decreases the number of OH− ligands and thus the number of potential bridging sites for dehydration reactions. This shall lead to the suppression of the edge-shared bonding probability and thus the tendency to form the rutile phase.[50,54] However, when a certain amount of HF is added to the HCl solution, the phase transformation from rutile to anatase occurs. Conceivably, HF can play dual roles here. On one hand, HF serves as a facet-controlling agent in stabilizing the (001) facets of anatase. On the other hand, HF acts as a ligand to form H_2TiF_6 with Ti4+ in the strongly acidic solution. This species could promote the bridge formation with H_2O due to the strong electronegativity of the F− ion, and subsequently dehydration occurs. In this case, the probability of edge-shared bonding is enhanced, which is beneficial to the formation of the anatase phase.[54,55] Nevertheless, the surface chemistry and the detailed mechanism of the morphology and phase evolution of the TiO_2 mesoporous single crystals with controllable crystallographic facets still need further investigation.

Effect of Seeding Concentrations. Apart from the hydrohalic acid reaction media, seeding concentration is another important factor in controlling the size and shape of the mesoporous TiO_2 single crystals. As clearly shown in Figure 3, large sizes of mesoporous branched nanorods (Figure 3a) and a mixture of olive-shaped mesoporous TiO_2 together with mesoporous nanosheets (Figure 3b) were obtained at the low seeding concentration (0.03 mM), whereas the high seeding concentration (15 mM) yielded small sizes of mesoporous thin
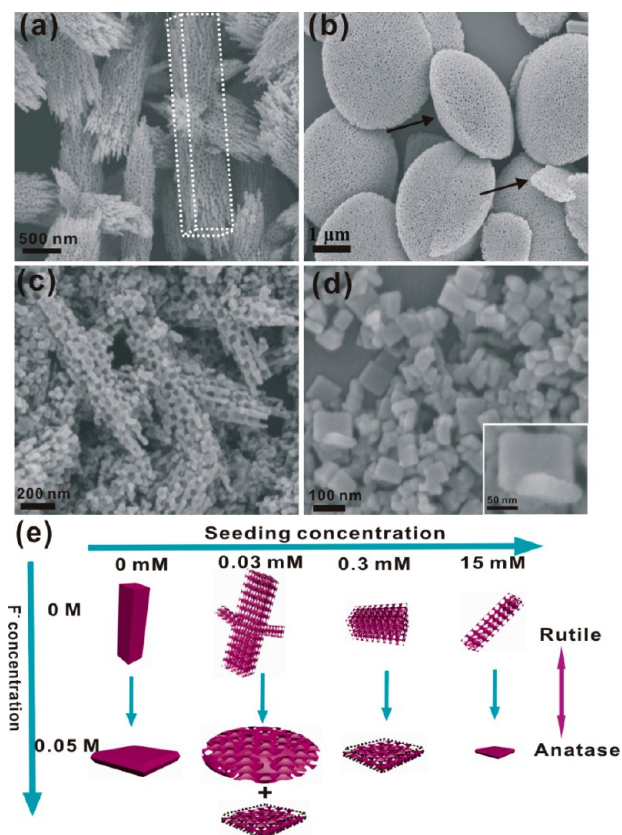

Figure 3. SEM images of (a) mesoporous TiO_2 branched nanorods (seeding concentration: 0.03 mM), (b) the mixture of olive-shaped mesoporous TiO_2 and mesoporous nanosheets (seeding concentration: 0.03 mM, HF: 0.05 M), (c) mesoporous TiO_2 thin nanorods (seeding concentration: 15 mM), and (d) nonporous TiO_2 nanosheets (seeding concentration: 15 mM, HF: 0.05 M). (e) The morphology and size evolution of solid and TiO_2 MSCs at different concentrations of HF and with different seeding concentrations.

nanorods with some fragments (Figure 3c) and nonporous nanosheets (Figure 3d). The size evolution of the TiO_2 products as a function of seeding concentrations was illustrated in Figure S3 (Supporting Information). In general, the size of the TiO_2 products is found to decrease with the increase of seeding concentration, which demonstrates explicitly that the mesoporous TiO_2 domain sizes depend more on the seeding concentrations rather than the pore dimension of the silica template as in the silica-templated themolysis methods.[46,47] Moreover, it is interesting to note that the sizes of the mesoporous TiO_2 crystals obtained at low seeding concentration are even larger than those of the solid single crystals, showing that the silica template is a better crystal growth media than the bulk solution due presumably to the less external interference.

As mentioned above, the shape of mesoporous TiO_2 products basically follows that of the solid TiO_2 products prepared under the same reaction conditions: nanorods were obtained in the HCl system, and nanosheets were obtained when HF was used. Essentially, the process of crystal growth appears to be independent of the template morphology. Referring to Figure 1 and Figure 3, it can be inferred that the seeding concentration plays a primary role in controlling the size as well as the shape of the mesoporous TiO_2 single crystals. When the seeding concentration was low, relatively large amounts of the Ti^{4+} precursor can take part in the growth around each nucleation site, and there was ample seed-to-seed spacing throughout the template, resulting in the large size of mesoporous TiO_2 crystals with some interesting crystal structures such as mesoporous branched-nanorod-shaped (Figure 3a) and olive-shaped (Figure 3b) crystals. When the seeding concentration was increased, the amount of the Ti^{4+} precursor available for each nucleation site as well as the seed-to-seed spacing were decreased, and hence smaller sizes of mesoporous TiO_2 crystals were produced. Finally, when the seeding concentration was further increased, much smaller mesoporous TiO_2 crystals, even nanosized nonporous TiO_2 single crystals, were obtained owing to the limited Ti^{4+} precursor supply for each nucleation site and the small seed-to-seed spacing (Figure 3c,d). To demonstrate the indispensability of the $TiCl_4$ seeding, we performed a control experiment by using a nonseeded silica template for the reaction. It was found that a majority of the TiO_2 crystals nucleated and grew in the bulk solution instead of growing inside the silica template, resulting in mostly the nonporous products and only very few mesoporous crystal products (see Figure S4 in the Supporting Information).

XRD patterns, TEM images, SAED patterns, and the related HRTEM images (see Figures S5−S8 in the Supporting Information) further revealed the tunable phases and the single-crystal nature of the MSCs with well-defined crystal facets, where rutile mesoporous nanorod single crystals were obtained in the HCl system and the shape and phase transformation from rutile nanorod to anatase nanosheets evolves when the HF was added. Exceptionally, the XRD pattern of mesoporous TiO_2 obtained at low seeding concentration (0.03 mM) exhibited rutile and anatase mixed phase rather than the pure anatase phase when HF was added (Figure S5b, Supporting Information). The detailed TEM and corresponding SAED patterns reveal that the large size of olive-shaped mesoporous TiO_2 single crystals shows rutile phase together with a small amount of mesoporous anatase nanosheet single crystals (Figure S6, Supporting Information), and only

mesoporous anatase nanosheets existed when HF concentration was increased to 0.1 M (see Figure S9 in the Supporting Information), indicating F^- played the key role for the phase transformation from rutile to anatase. For convenience, hereafter, we designate various TiO_2 structures as "X−SC (MSC)−C", where X refers to the phase of TiO_2 (R for rutile and A for anatase), SC (MSC) is denoted as single crystal or mesoporous single crystal, and C is the $TiCl_4$ seeding concentration.

The detailed morphology, size, and phase evolutions were summarized in Figure 3e. It is shown clearly that two elements are keys to the successful growth of shape- and size-controlled R-MSCs and A-MSCs, i.e., the strong hydrohalic acid hydrothermal system and the $TiCl_4$ seeding treatment. First, the use of hydrohalic acid media as morphology and phase controlling agents favors the formation of R-MSCs and A-MSCs with well-defined facets;[42,43,50,51] i.e., MSCs form [001]-oriented tetragonal rutile mesoporous nanorods at high concentration of HCl and evolve anatase mesoporous nanosheets with dominant {001} facets when adding a small quantity of HF. Second, the $TiCl_4$ pretreatment facilitates TiO_2 single crystals to heterogeneously nucleate and grow within the silica template, generating uniform mesopores negatively replicating the silica template. Moreover, different seeding concentrations result in diverse morphologies and sizes of TiO_2 MSCs that influence local Ti^{4+} precursor concentration and seed-to-seed spacing in the silica template. Specifically, large sizes of TiO_2 MSCs were obtained at low seeding concentrations because relatively large amounts of the Ti^{4+} precursor can take part in the growth around each nucleation site, and there was ample seed-to-seed spacing throughout the template. When the seeding concentration was increased, however, smaller sizes of TiO_2 MSCs were produced, owing to the less amount of Ti^{4+} precursor avaliable for each nucleation site and the smaller seed-to-seed spacing. Thus when seeding concentration was high, MSCs of small sizes, even nanosized nonporous TiO_2 single crystals, were obtained.

Nitrogen adsorption−desorption isotherms of the selected samples together with the corresponding pore-size distributions were shown in Figure 4 and Figure S10 in the Supporting
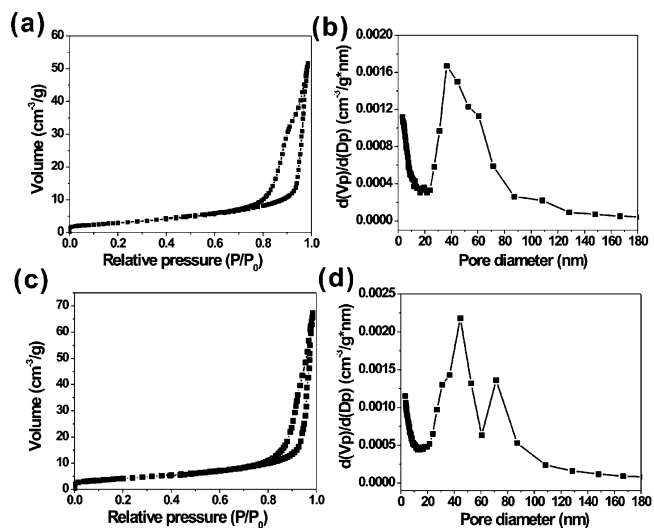
Figure 4. N$_2$ adsorption−desorption isotherms and the corresponding pore size distribution derived from adsorption isotherm of (a, b) R-MSC-0.3 and (c, d) A-MSC-0.3 (HF: 0.05 M).

Information. The mesoporous single crystals show type-IV isotherms and exhibit a broad hysteresis loop, which is characteristic of mesoporous materials.[56,57] The mesoporous single crystals exhibit relatively narrow pore size distributions with an average pore diameter of 50 nm, in agreement with the value observed from SEM and TEM images. BET specific surface areas of these TiO_2 products were listed in Table 1. The

Table 1. BET Specific Surface Area of the TiO_2 Products

sample	S_{BET} (m^2 g^{-1})	sample	S_{BET} (m^2 g^{-1})
R-SC	7.00	A-SC	2.89
R-MSC-0.03	9.76	R+A-MSC-0.03	14.92
R-MSC-0.3	11.22	A-MSC-0.3	15.62
R-MSC-15	33.20	A-SC-15	37.98
P25	56.51		

specific surface areas of mesoporous single crystals obtained at different seeding concentrations are generally larger than those of the solid TiO_2 crystals but still smaller than that of P25 due to their relatively large mesopores and crystal sizes. By reducing the silica sphere size, one should be able to increase the surface area of the mesoporous single crystals, which is under investigation in our laboratory.

Effect of Hydrothermal Treatment Temperature. As an alternative to the seeding concentration, reaction temperature can also be varied to control the sizes of the TiO_2 MSCs (Figure 5). We first look at the situation of a low seeding concentration (0.03 mM). For the rutile products, large sized, branched-rod-shaped MSCs (~1−1.5 μm in width, ~5 μm in

Figure 5. SEM images of (a) R-MSC-0.03 (180 °C), (b) R-MSC-0.03 (200 °C), (c) R-MSC-0.3 (180 °C), (d) R-MSC-0.3 (150 °C), (e) A-MSC-0.3 (HF: 0.05 M, 180 °C), and (f) A-MSC-0.3 (HF: 0.05 M, 150 °C).

length) were obtained when the hydrothermal treatment temperature was 200 °C (Figure 5b), whereas considerably smaller sized MSCs were obtained at 180 °C (average width of ~700−900 nm and length of ~3−4 μm) (Figure 5a). Similarly, with a seeding concentration of 0.3 mM, smaller sizes of nanorod-shaped MSCs were obtained (Figure 5d, ~300−350 nm in width, ~400 nm in length) at 150 °C than those at 180 °C (Figure 5c, average width of ~300−400 nm and length of ~500−600 nm). Such temperature dependency also holds for the situation of the anatase products. For example, the anatase mesoporous nanosheets obtained at 150 °C (Figure 5f, average width of ~500−600 nm and thickness of ~100 nm) are smaller than those at 180 °C (Figure 5e, average width of ~700−800 nm and thickness of ~150 nm). This result clearly demonstrates that increasing the reaction temperature can effectively increase the size of the TiO_2 MSCs at a given seeding concentration and reaction time. A simple explanation lies in the increased reaction rate and thus crystal growth rate due to the nature of the activated process.[58,59] There is a limit to this trend, however, when the seeding concentration is too high, e.g., up to 15 mM; now the sizes of MSCs are almost unchanged with the growth temperature (see Figure S11 in the Supporting Information). In such a high seeding concentration regime, the seeding concentration predominates in the control of the sizes of MSCs.

The results presented above point to an interesting scenario that the morphology, size, and phase of the resultant mesoporous TiO_2 single crystals depend more on the external conditions such as reaction solution media, seeding concentration, and growth temperature rather than on the silica template itself. In other words, the silica templates are rather dutiful in the sense that they allow faithful negative replication but without interfering in the crystallization process. Moreover, the silica template used in this work provides several additional advantages: (1) it is facile to fabricate highly monodisperse silica particles with controllable size,[60] meaning that the internal mesopore size and the resulting surface area are adjustable by using silica templates of different diameters; (2) the peculiar colloidal properties of the silica beads make it easy to form quasi-close-packed templates by simple centrifugation and calcination; (3) the high hydrophilicity of the internal surfaces full of hydroxyl groups facilitates the seeding of TiO_2 nucleation sites on the silica templates and the guiding of the subsequent growth;[61] (4) the silica templates can be readily removed after templating reactions by NaOH or HF solutions without the need of high-temperature calcination, thereby maintaining the integrity of the mesoporous structures; and (5) last but not least, the apparent insensitivity of the overall morphological characteristics of the obtained mesoporous single crystals to the silica templates provides a handle to tune the structure of the TiO_2 MSCs by changing the external conditions and attests the universality of the template method for the synthesis of other MSCs beyond TiO_2.

Photocatalytic Activities of Rutile and Anatase Mesoporous TiO_2 Single Crystals. Owing to the three-dimensionally connected mesoporous architecture and the single-crystal nature of the TiO_2 MSCs, charge transport from the bulk to surface is expected to quicken, and this can help to alleviate recombination between the photogenerated electrons and holes, thereby greatly improving the photocatalytic activities of TiO_2 MSCs.[62−65] To confirm this, we investigated the reductive and oxidative photocatalytic activities of the R-MSCs and A-MSCs. Figure 6a and Figure S12a (see Supporting
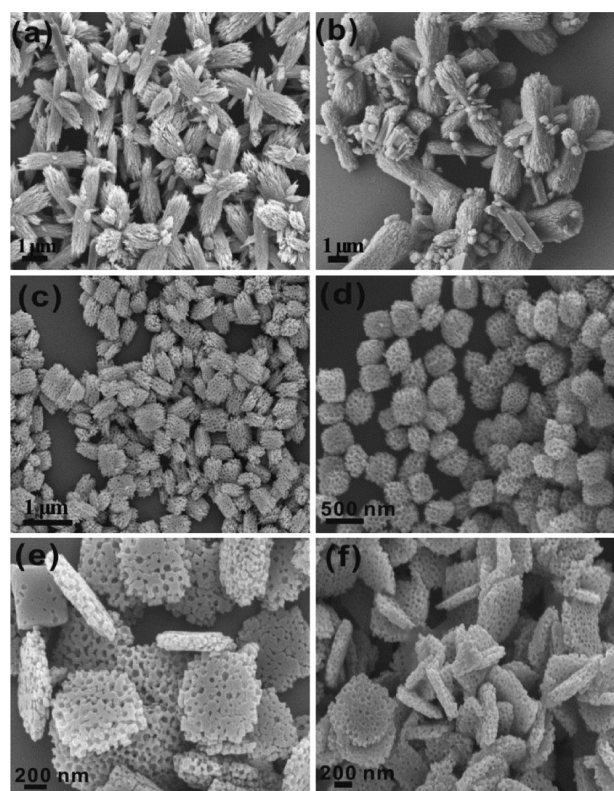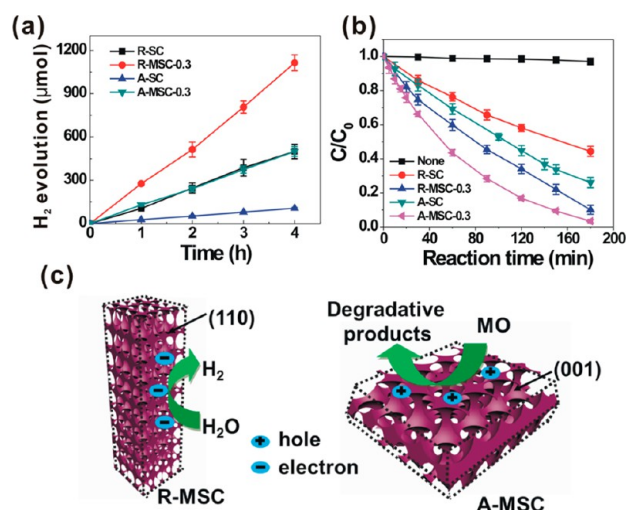
Figure 6. (a) Hydrogen evolution curves of R-SC, R-MSC-0.3, A-SC (HF: 0.05 M), and A-MSC-0.3 (HF: 0.05 M). (b) Methyl orange (MO) degradation versus irradiation time in the presence of R-SC, R-MSC-0.3, A-SC (HF: 0.05 M), and A-MSC-0.3 (HF: 0.05 M), respectively. (c) The mechanism of photoreduction for hydrogen evolution on R-MSCs and photoxidation MO degradation on A-MSCs, respectively. Error bars represent the standard deviations of the measured data points (based on three as-prepared samples).

Information) showed photocatalytic hydrogen evolution curves of the TiO$_2$ MSCs together with the solid single crystals as a function of irradiation time. For comparison, the photocatalytic performance of commercial P25 was also tested. The hydrogen evolution rates were summarized in Table S1 (Supporting Information). As shown in Figure 6a, the hydrogen evolution rates of the R-MSCs and A-MSCs are both much higher than those of the corresponding solid single crystals, confirming the positive effect of their increased surface area and the more efficient charge separation and transport in the porous single crystals. It is noteworthy that the R-MSCs prepared at the high seeding concentration (15 mM) exhibit even higher photocatalytic activity than that of P25 (Figure S12a and Table S1, Supporting Information) in spite of its relatively lower specific surface area (Table 1). P25 was known to be an excellent TiO$_2$ photocatalyst due to the small particle size and the presence of both anatase and rutile.[66] So the result clearly indicates that the single crystalline nature of the porous MSCs has contributed to the high photocatalytic activity due to fast charge transport and low recombination.

To further evaluate their photocatalytic activities, we also performed photocatalytic decomposition of methyl orange (MO) as a probe reaction under the irradiation of a 300 W Xe lamp (with the wavelength of 320−780 nm). Figure 6b and Figure S12b (Supporting Information) show the photodegradation efficiency of MO versus irradiation time, which was estimated by examining the variation of the characteristic adsorption peak intensity of MO at 465 nm. In the absence of the photocatalyst, the MO was hardly decomposed, although the condition was otherwise identical. Clearly, the TiO$_2$ MSC samples show remarkably higher efficiencies (90% for R-MSC-0.3 and 97% for A-MSC-0.3) in the photocatalytic degradation of MO than the corresponding solid single crystals (56% for R-SC and 74% for A-SC) after the irradiation of a 300 W Xe lamp for 180 min (Figure 6b). Significantly, the existence of the mesoporous structure has allowed not only the effective charge

transport and separation but also the rapid diffusion of reactants and products.[67]

Apart from the surface area and crystallinity, the photocatalytic activities of TiO$_2$ are also strictly related to the many other factors, such as band gap structure, photoexcited electron−hole (e−h) lifetime, and external exposed crystal facets.[68,69] In general, anatase crystals exhibit higher photocatalytic activity than rutile ones since the anatase possesses higher Fermi level, longer photoexcited electron−hole lifetime, and higher electron mobility.[70,71] Interestingly, the R-MSCs and A-MSCs show distinctly different photocatalytic activities; that is, the rutile crystals show higher reductive photocatalytic activity (9005 μmol h^{-1} g^{-1} for R-MSC-0.3 and 4158 μmol h^{-1} g^{-1} for A-MSC-0.3), while the anatase ones exhibit better oxidative photocatalytic activity (90% for R-MSC-0.3 and 97% for A-MSC-0.3 after the irradiation for 180 min) (Figure 6). The different photocatalytic activities of the TiO$_2$ MSCs may be ascribed to the different exposed crystal facets. The role of crystal facets in the photocatalytic processes has been intensively studied. Each crystal facet owns its unique surface atomic arrangement and electronic configuration and thus results in different photocatalytic properties.[72−74] Many experimental results have shown that rutile {001} or {111} facets and anatase {001} facets provide the sites for oxidation, while the rutile {110} and anatase {101} facets offer the sites for reduction,[72,75−78] and theoretical calculations have also indicated that adsorption and dissociation of the water molecule is energetically favored on the rutile {110} facets and anatase {101} facets.[79] Therefore, the high reductive photocatalytic activity of the rutile MSCs we observed can be ascribed to the effective reduction sites provided by the abundantly exposed {110} facets, while the preferentially exposed {001} facets of the anatase MSCs are responsible for the high oxidative photocatalytic activity. As depicted in Figure 6c, the {110} facets of R-MSCs provide reduction sites for hydrogen evolution, while the {001} facets of A-MSCs are the oxidation sites for MO degradation. Clearly, the enhancement of photocatalytic activity can be mainly ascribed to the increased surface area, single crystal nature, and the exposure of reactive crystal facets coupled with the three-dimensionally connected mesoporous architecture of the TiO$_2$ MSCs.

■ CONCLUSIONS

In summary, the silica-templated hydrothermal method has been demonstrated to be a facile approach to the shape-, size-, and phase-controlled synthesis of R-MSCs and A-MSCs. Our systematic studies have led to a plausible in-template crystal growth model, which involves heterogeneous crystal nucleation from the preformed nucleation sites and oriented growth of TiO$_2$ crystals by filling the void spaces. A series of mesoporous single-crystal structures, including rutile mesoporous TiO$_2$ nanorods with tunable sizes and anatase mesoporous TiO$_2$ nanosheets with dominant {001} facets, have been synthesized to demonstrate the versatility of the strategy. The morphology, size, and phase of the TiO$_2$ MSCs were found to be virtually independent of the silica template, in much the same way as in the solution synthesis of the solid single-crystal counterpart but with an added advantage of less aggregation. In other words, the attributes of the MSCs could be simply adjusted by changing the external conditions (precursor solution, seeding density, growth temperature, etc.), demonstrating the universality of the template method for the synthesis of other mesoporous single crystals beyond TiO$_2$. On the application

side, the resultant TiO$_2$ MSCs exhibited remarkable photo-catalytic performance on both photoreductive activity for hydrogen evolution and photooxidative activity for the degradation of MO, which could be largely attributed to their increased surface area, single-crystal nature, and the exposure of reactive crystal facets coupled with the three-dimensionally connected mesoporous architecture. Further improvement in the photocatalytic activity should be possible by increasing their surface area and modifying their electronic and optical properties by doping or by forming heterojunction structures.

■ ASSOCIATED CONTENT

Ⓢ Supporting Information

SEM characterization of the silica template, TEM and SEM images of TiO$_2$ products obtained at different conditions, size evolution of the TiO$_2$ MSCs as a function of seeding concentration, nitrogen adsorption−desorption isotherm and pore-size distribution of TiO$_2$ products obtained at different conditions, and photocatalytic performances of the TiO$_2$ MSCs. This material is available free of charge via the Internet at http://pubs.acs.org.

■ AUTHOR INFORMATION

Corresponding Author
*E-mail: chsyang@ust.hk.

Notes
The authors declare no competing financial interest.

■ ACKNOWLEDGMENTS

■ REFERENCES

(1) Li, D. L.; Zhou, H. S.; Honma, I. *Nat. Mater.* **2004**, *3*, 65−72.

(2) Kondo, J. N.; Domen, K. *Chem. Mater.* **2008**, *20*, 835−847.

(3) Wan, Y.; Yang, H. F.; Zhao, D. Y. *Acc. Chem. Res.* **2006**, *39*, 423−432.

(4) Yue, W. B.; Zhou, W. Z. *Prog. Nat. Sci.* **2008**, *18*, 1329−1338.

(5) Lee, J.; Orilall, M. C.; Warren, S. C.; Kamperman, M.; Disalvo, F. J.; Wiesner, U. *Nat. Mater.* **2008**, *7*, 222−228.

(6) Mandlmeier, B.; Szeifert, J. M.; Fattakhova-Rohlfing, D.; Amenitsch, H.; Bein, T. *J. Am. Chem. Soc.* **2011**, *133*, 17274−17282.

(7) Ren, Y.; Ma, Z.; Bruce, P. G. *Chem. Soc. Rev.* **2012**, *41*, 4909−4927.

(8) Liu, F. J.; Zuo, S. F.; Xia, X. D.; Sun, J.; Zou, Y. C.; Wang, L.; Li, C. G.; Qi, C. Z. *J. Mater. Chem. A* **2013**, *1*, 4089−4096.

(9) Yang, P. D.; Zhao, D. Y.; Margolese, D. I.; Chmelka, B. F.; Stucky, G. D. *Nature* **1998**, *396*, 152−155.

(10) Wu, C. W.; Ohsuna, T.; Kuwabara, M.; Kuroda, K. *J. Am. Chem. Soc.* **2006**, *128*, 4544−4545.

(11) Tsung, C. K.; Fan, J.; Zheng, N. F.; Shi, Q. H.; Forman, A. J.; Wang, J. F.; Stucky, G. D. *Angew. Chem., Int. Ed.* **2008**, *47*, 8682−8686.

(12) Reitz, C.; Suchomski, C.; Weidmann, C.; Brezesinski, T. *Nano Res.* **2011**, *4*, 414−424.

(13) Zhang, J. Y.; Deng, Y. H.; Gu, D.; Wang, S. T.; She, L.; Che, R. C.; Wang, Z. S.; Tu, B.; Xie, S. H.; Zhao, D. Y. *Adv. Energy Mater.* **2011**, *1*, 241−248.

(14) Deng, Y. H.; Wei, J.; Sun, Z. K.; Zhao, D. Y. *Chem. Soc. Rev.* **2013**, *42*, 4054−4070.

(15) Zhang, Y.; Xie, Z. B.; Wang, J. *ACS Appl. Mater. Interfaces* **2009**, *1*, 2789−2795.

(16) Zhu, K. K.; Yue, B.; Zhou, W. Z.; He, H. Y. *Chem. Commun.* **2003**, 98−99.

(17) Jiao, F.; Harrison, A.; Jumas, J. C.; Chadwick, A. V.; Kockelmann, W.; Bruce, P. G. *J. Am. Chem. Soc.* **2006**, *128*, 5468−5474.

(18) Lu, A. H.; Schuth, F. *Adv. Mater.* **2006**, *18*, 1793−1805.

(19) Lai, X. Y.; Li, X. T.; Geng, W. C.; Tu, J. C.; Li, J. X.; Qiu, S. L. *Angew. Chem., Int. Ed.* **2007**, *46*, 738−741.

(20) Armatas, G. S.; Katsoulidis, A. P.; Petrakis, D. E.; Pomonis, P. J.; Kanatzidis, M. G. *Chem. Mater.* **2010**, *22*, 5739−5746.

(21) Shopsowitz, K. E.; Stahl, A.; Hamad, W. Y.; MacLachlan, M. J. *Angew. Chem., Int. Ed.* **2012**, *51*, 6886−6890.

(22) Serrano, D. P.; Escola, J. M.; Pizarro, P. *Chem. Soc. Rev.* **2013**, *42*, 4004−4035.

(23) Leshuk, T.; Linley, S.; Baxter, G.; Gu, F. *ACS Appl. Mater. Interfaces* **2012**, *4*, 6062−6070.

(24) Crepaldi, E. L.; Soler-Illia, G. J. D. A.; Grosso, D.; Cagnol, F.; Ribot, F.; Sanchez, C. *J. Am. Chem. Soc.* **2003**, *125*, 9770−9786.

(25) Dickinson, C.; Zhou, W. Z.; Hodgkins, R. P.; Shi, Y. F.; Zhao, D. Y.; He, H. Y. *Chem. Mater.* **2006**, *18*, 3088−3095.

(26) Yue, W. B.; Hill, A. H.; Harrison, A.; Zhou, W. Z. *Chem. Commun.* **2007**, 2518−2520.

(27) Yue, W. B.; Randorn, C.; Attidekou, P. S.; Su, Z. X.; Irvine, J. T. S.; Zhou, W. Z. *Adv. Funct. Mater.* **2009**, *19*, 2826−2833.

(28) Kang, M.; Kim, D.; Yi, S. H.; Han, J. U.; Yie, J. E.; Kim, J. M. *Catal. Today* **2004**, *93−95*, 695−699.

(29) Xu, H.; Reunchan, P.; Ouyang, S.; Tong, H.; Umezawa, N.; Kako, T.; Ye, J. *Chem. Mater.* **2013**, *25*, 405−411.

(30) Kowalski, D.; Kim, D.; Schmuki, P. *Nano Today* **2013**, *8*, 235−264.

(31) Hao, B.; Yan, Y.; Wang, X. B.; Chen, G. *ACS Appl. Mater. Interfaces* **2013**, *5*, 6285−6291.

(32) Ni, M.; Leung, M. K. H.; Leung, D. Y. C.; Sumathy, K. *Renew. Sust. Energy Rev.* **2007**, *11*, 401−425.

(33) Gratzel, M. *Nature* **2001**, *414*, 338−344.

(34) Chen, X.; Mao, S. S. *Chem. Rev.* **2007**, *107*, 2891−2959.

(35) Ren, Y.; Liu, Z.; Pourpoint, F.; Armstrong, A. R.; Grey, C. P.; Bruce, P. G. *Angew. Chem., Int. Ed.* **2012**, *51*, 2164−2167.

(36) Brezesinski, T.; Wang, J.; Polleux, J.; Dunn, B.; Tolbert, S. H. *J. Am. Chem. Soc.* **2009**, *131*, 1802−1809.

(37) Szeifert, J. M.; Fattakhova-Rohlfing, D.; Georgiadou, D.; Kalousek, V.; Rathousky, J.; Kuang, D.; Wenger, S.; Zakeeruddin, S. M.; Gratzel, M.; Bein, T. *Chem. Mater.* **2009**, *21*, 1260−1265.

(38) Szeifert, J. M.; Feckl, J. M.; Fattakhova-Rohlfing, D.; Liu, Y. J.; Kalousek, V.; Rathousky, J.; Bein, T. *J. Am. Chem. Soc.* **2010**, *132*, 12605−12611.

(39) Ye, J. F.; Liu, W.; Cai, J. G.; Chen, S. A.; Zhao, X. W.; Zhou, H. H.; Qi, L. M. *J. Am. Chem. Soc.* **2011**, *133*, 933−940.

(40) Docampo, P.; Guldin, S.; Steiner, U.; Snaith, H. J. *J. Phys. Chem. Lett.* **2013**, *4*, 698−703.

(41) Imanishi, A.; Suzuki, H.; Murakoshi, K.; Nakato, Y. *J. Phys. Chem. B* **2006**, *110*, 21050−21054.

(42) Liu, B.; Aydil, E. S. *J. Am. Chem. Soc.* **2009**, *131*, 3985−3990.

(43) Yang, H. G.; Sun, C. H.; Qiao, S. Z.; Zou, J.; Liu, G.; Smith, S. C.; Cheng, H. M.; Lu, G. Q. *Nature* **2008**, *453*, 638−642.

(44) Wu, X.; Chen, Z. G.; Lu, G. Q.; Wang, L. Z. *Adv. Funct. Mater.* **2011**, *21*, 4167−4172.

(45) Bian, Z. F.; Zhu, J. A.; Wen, J.; Cao, F. L.; Huo, Y. N.; Qian, X. F.; Cao, Y.; Shen, M. Q.; Li, H. X.; Lu, Y. F. *Angew. Chem., Int. Ed.* **2011**, *50*, 1105−1108.

(46) Yue, W. B.; Xu, X. X.; Irvine, J. T. S.; Attidekou, P. S.; Liu, C.; He, H. Y.; Zhao, D. Y.; Zhou, W. Z. *Chem. Mater.* **2009**, *21*, 2540−2546.

(47) Crossland, E. J. W.; Noel, N.; Sivaram, V.; Leijtens, T.; Alexander-Webber, J. A.; Snaith, H. J. *Nature* **2013**, *495*, 215−219.

(48) Park, N. G.; van de Lagemaat, J.; Frank, A. J. *J. Phys. Chem. B* **2000**, *104*, 8989−8994.

(49) Wang, D. H.; Choi, D. W.; Yang, Z. G.; Viswanathan, V. V.; Nie, Z. M.; Wang, C. M.; Song, Y. J.; Zhang, J. G.; Liu, J. *Chem. Mater.* **2008**, *20*, 3435−3442.

(50) Yanagisawa, K.; Ovenstone, J. *J. Phys. Chem. B* **1999**, *103*, 7781−7787.

(51) Guo, W. X.; Zhang, F.; Lin, C. J.; Wang, Z. L. *Adv. Mater.* **2012**, *24*, 4761−4764.

(52) Wu, L.; Yang, B. X.; Yang, X. H.; Chen, Z. G.; Li, Z.; Zhao, H. J.; Gong, X. Q.; Yang, H. G. *CrystEngComm* **2013**, *15*, 3252−3255.

(53) Lai, Z. C.; Peng, F.; Wang, H. J.; Yu, H.; Zhang, S. Q.; Zhao, H. J. *J. Mater. Chem. A* **2013**, *1*, 4182−4185.

(54) Cheng, H. M.; Ma, J. M.; Zhao, Z. G.; Qi, L. M. *Chem. Mater.* **1995**, *7*, 663−671.

(55) Zhang, H. M.; Wang, Y.; Liu, P. R.; Han, Y. H.; Yao, X. D.; Zou, J.; Cheng, H. M.; Zhao, H. J. *ACS Appl. Mater. Interfaces* **2011**, *3*, 2472−2478.

(56) Yang, P. D.; Zhao, D. Y.; Margolese, D. I.; Chmelka, B. F.; Stucky, G. D. *Chem. Mater.* **1999**, *11*, 2813−2826.

(57) Zhang, H. J.; Du, G. D.; Lu, W. Q.; Cheng, L. L.; Zhu, X. F.; Jiao, Z. *CrystEngComm* **2012**, *14*, 3793−3801.

(58) De Yoreo, J. J.; Vekilov, P. G. *Rev. Mineral. Geochem.* **2003**, *54*, 57−93.

(59) Cho, I. S.; Chen, Z. B.; Forman, A. J.; Kim, D. R.; Rao, P. M.; Jaramillo, T. F.; Zheng, X. L. *Nano Lett.* **2011**, *11*, 4978−4984.

(60) Bogush, G. H.; Tracy, M. A.; Zukoski, C. F. *J. Non-Cryst. Solids* **1988**, *104*, 95−106.

(61) Ennaoui, A.; Sankapal, B. R.; Skryshevsky, V.; Lux-Steiner, M. C. *Sol. Energy Mater. Sol. Cells* **2006**, *90*, 1533−1541.

(62) Ducati, C. *Nature* **2013**, *495*, 180−181.

(63) Kuang, Q.; Yang, S. H. *ACS Appl. Mater. Interfaces* **2013**, *5*, 3683−3690.

(64) Parlett, C. M. A.; Wilson, K.; Lee, A. F. *Chem. Soc. Rev.* **2013**, *42*, 3876−3893.

(65) Wang, J. G.; Bian, Z. F.; Zhu, J.; Li, H. X. *J. Mater. Chem. A* **2013**, *1*, 1296−1302.

(66) Hurum, D. C.; Agrios, A. G.; Gray, K. A.; Rajh, T.; Thurnauer, M. C. *J. Phys. Chem. B* **2003**, *107*, 4545−4549.

(67) Zhang, A. Y.; Long, L. L.; Li, W. W.; Wang, W. K.; Yu, H. Q. *Chem. Commun.* **2013**, *49*, 6075−6077.

(68) Kubacka, A.; Fernandez-Garcia, M.; Colon, G. *Chem. Rev.* **2012**, *112*, 1555−1614.

(69) Osterloh, F. E. *Chem. Soc. Rev.* **2013**, *42*, 2294−2320.

(70) Banerjee, S.; Gopal, J.; Muraleedharan, P.; Tyagi, A. K.; Rai, B. *Curr. Sci. India* **2006**, *90*, 1378−1383.

(71) Xu, M. C.; Gao, Y. K.; Moreno, E. M.; Kunst, M.; Muhler, M.; Wang, Y. M.; Idriss, H.; Woll, C. *Phys. Rev. Lett.* **2011**, *106*, 138302.

(72) D'Arienzo, M.; Carbajo, J.; Bahamonde, A.; Crippa, M.; Polizzi, S.; Scotti, R.; Wahba, L.; Morazzoni, F. *J. Am. Chem. Soc.* **2011**, *133*, 17652−17661.

(73) Pan, J.; Liu, G.; Lu, G. M.; Cheng, H. M. *Angew. Chem., Int. Ed.* **2011**, *50*, 2133−2137.

(74) Xu, H.; Reunchan, P.; Ouyang, S. X.; Tong, H.; Umezawa, N.; Kako, T.; Ye, J. H. *Chem. Mater.* **2013**, *25*, 405−411.

(75) Ohno, T.; Sarukawa, K.; Matsumura, M. *New J. Chem.* **2002**, *26*, 1167−1170.

(76) Murakami, N.; Katayama, S.; Nakamura, M.; Tsubota, T.; Ohno, T. *J. Phys. Chem. C* **2011**, *115*, 419−424.

(77) Murakami, N.; Kurihara, Y.; Tsubota, T.; Ohno, T. *J. Phys. Chem. C* **2009**, *113*, 3062−3069.

(78) Liu, L.; Gu, X.; Ji, Z.; Zou, W.; Tang, C.; Gao, F.; Dong, L. *J. Phys. Chem. C* **2013**, *117*, 18578−18587.

(79) Schaub, R.; Thostrup, P.; Lopez, N.; Laegsgaard, E.; Stensgaard, I.; Norskov, J. K.; Besenbacher, F. *Phys. Rev. Lett.* **2001**, *87*, 266104.

11257

dx.doi.org/10.1021/am403482g | *ACS Appl. Mater. Interfaces* 2013, 5, 11249−11257